

Mixed higher-order topology and nodal and nodeless flat band topological phases in a superconducting multiorbital model

Rodrigo Arouca¹, Tanay Nag^{2,1,*} and Annica M. Black-Schaffer¹

¹*Department of Physics and Astronomy, Uppsala University, 75120 Uppsala, Sweden and*

²*Department of Physics, BITS Pilani-Hyderabad Campus, Telangana 500078, India*

(Dated: February 2, 2024)

We investigate the topological phases that appear in an orbital version of the Benalcazar-Bernevig-Hughes (BBH) model in the presence of conventional spin-singlet s -wave superconductivity and with the possibility of tuning an in-plane magnetic field. We chart out the phase diagram by considering different boundary conditions, with the topology of the individual phases further examined by considering both the Wannier and entanglement spectra, as well as the Majorana polarization. For weak to moderate values of magnetic field and superconducting pairing amplitude, we find a second-order topological superconductor phase with eight zero-energy corner modes. Further increasing field or pairing, half of the corner states can be turned into zero-energy edge-localized modes, thus forming a type of hybrid-order phase. Then, we find two different putative first-order topological phases, a nodal and a nodeless phase, both with zero-energy flat bands localized along mirror-symmetric open edges. For the nodal phase, the flat bands are localized between the nodes in reciprocal space, while in the nodeless phase, with its a full bulk gap, the zero-energy boundary flat band spans the whole Brillouin zone.

I. INTRODUCTION

The study of topological materials is an extremely active area of research in condensed matter physics. They present phases of matter that are not characterized by spontaneous symmetry breaking but rather by topological invariants. In the Altland-Zirnbauer classification [1, 2], time-reversal, particle-hole, and chiral symmetries classify ten possible topological classes, indicating the kind of invariant and the branches of the symmetry-protected boundary states. The number of possible symmetry-protected topological classes of free fermions has further been increased by including crystalline symmetries to this original classification [3–7].

In addition to new topological classes, crystalline symmetries also allow for the presence of higher-order topological phases [8–11], where the topological invariant computed in the bulk is not related to modes appearing on the whole surface of the material but rather on a smaller set. As an example, the original model of a higher-order topological insulator, the two-dimensional (2D) Benalcazar-Bernevig-Hughes (BBH) model [8, 9], hosts a second-order topological phase with protected zero-energy modes appearing at the corners of the system. The last years have seen a profusion of work on higher-order topological insulators [12–23], with experimental realization in materials [11, 24] and a variety of metamaterials [25–33].

A particularly interesting class of higher-order topological systems is composed of higher-order topological superconductors (HOTSC), both for static and driven Hamiltonians [34–42]. The corner or hinge states in HOTSC appear at zero energy and can, as such, host

Majorana zero modes (MZMs) [43–50], where their spatial separation can be controlled and degree of degeneracy can also be tuned under certain circumstances. As such, they must present an equal amount of particle and hole components and are thus their own antiparticles, which are promising for applications in quantum computing due to their non-Abelian properties [51]. Topologically protected boundary states can also appear in nodal superconductors [52–59]. Topological nodal superconductor is a non-trivial phase that is not contained in the Altland-Zirnbauer classification since the bulk of the system is gapless at the nodal points [54, 55, 57]. Nevertheless, the presence of the nodal points is protected by symmetry, and there exists a bulk-boundary correspondence between the topology of the bulk nodal points and boundary-localized flat bands located between the nodes. It would be interesting to uncover systems where multiple different superconducting topological phases are readily realized, including higher-order topology or various nodal states. This would not only give realizations of the individual topological phases, and possible intriguing combinations thereof, but also offer tunability between the different phases and their characteristic properties as well as the possibility to uncover previously unknown phases.

In this work, we set out to study a simple and versatile superconducting model, and we find a plethora of different topological phases. Aiming at least for higher-order topology, we choose to investigate the orbital version of the BBH model in the deep topological limit with conventional spin-singlet s -wave superconductivity induced by proximity effect from a substrate and using an applied in-plane magnetic field as an additional easily accessible tunable parameter, all illustrated in Fig. 1(a). The in-plane magnetic field B_x breaks the C_4 symmetry responsible for protecting the corner states in the BBH model, while the proximity-induced superconducting order pa-

* tanay.nag@hyderabad.bits-pilani.ac.in

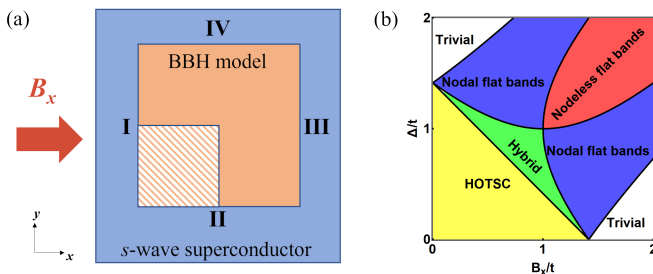


FIG. 1. (a) Schematic realization of the superconducting BBH model: BBH system with conventional spin-singlet s -wave superconducting pairing Δ induced by proximity effect from a substrate and an in-plane magnetic field B_x . Different edges are indicated by Roman numerals. Dashed area represents the region where the entanglement spectrum is computed. (b) Summary of phase diagram: Solid lines represent analytical expressions for the phase boundaries, while different colors represent different topological phases. See main text for further definitions.

parameter Δ transforms these states in electron-hole excitations. Moreover, we find that the superconducting term in this orbital model is represented by an unusual matrix structure, giving rise to a multitude of different topological phases. Using the Wannier spectrum [7, 9, 11], the entanglement spectrum [60–64] for a quarter of the lattice indicated as in Fig. 1(a), and the Majorana polarization [65, 66], we completely characterize the topological phases and obtain the rich phase diagram in Fig. 1(b).

To briefly summarize the phase diagram, for $B_x = 0$ and $\Delta \approx 0$ the result is the superconducting version of the second-order topological phase of the BBH model characterized by eight corner states and shown as the HOTSC phase (yellow) in Fig. 1(b). The pairing makes the corner states of the BBH model transform into Andreev bound states (ABS), built up from two degenerate MZMs, located at each corner. The presence of both finite pairing and an in-plane magnetic field makes even more interesting topological phases appear. For larger values of both Δ and B_x we first find another higher-order topological phase, a type of hybrid ordered phase (green). In this phase, some (four) of the original zero-energy corner states stay, becoming isolated MZMs, while the rest turn into MZMs localized along in the y -direction, edges II and IV, in Fig. 1(a). This presents an intriguing mix, or hybrid, of a second-order and a dipolar topological phase, but where the number edge localized states do not grow with system size as usually expected. Further increasing B_x and Δ , we find two other interesting topological phases. These are both first-order topological phases with flat bands at zero energy. One of the phases is more traditional, a nodal flat band phase (blue). Here the bulk of the system is gapless with symmetry-protected nodes and the zero-energy flat bands localized on the y -edge, occur in the region of momentum space between the nodes, as expected for a topological nodal superconductor. However, in the other topological flat

band phase the bulk stays completely gapped, but we nevertheless find flat bands at zero energy, now spanning across the whole Brillouin zone and localized at the edges along the x -direction, which we name a nodeless flat band phase (red). The association of these flat bands to a bulk invariant remains unclear, but we find that they clearly appear in a quantized Wannier spectrum. Both flat band phases present four zero-energy states per momenta, two at each edge, with a large Majorana polarization, such that we consider them to be MZMs. These results show how a seemingly simple model can generate a plethora of topological phases, accessible by tuning physical parameters. Importantly, the results further establish the existence of both a hybrid-order phase and a fully gapped (i.e. nodeless) topological phase with zero-energy flat bands boundary states.

The rest of this work is structured as follows. In Sec. II we briefly summarize the main properties of the BBH model and discuss the form of the Hamiltonian, especially the superconducting pairing and the magnetic field term, which we add to the BBH model. In Sec. III we introduce the three topological invariants we use in this work, explaining what aspects of topological phases can be characterized by each invariant. In Sec. IV we report our main results. First, we consider gap closings as a function of Δ and B_x , which indicate the phase boundaries. For each phase, we analyze the behavior of the energy spectra for different boundary conditions as well as the different topological invariants, in order to characterize all phases. In Sec. V we discuss the dual [67] and surface [35, 59] Hamiltonians for this model, which help us understand the presence of nodes starting with s -wave pairing and the higher-order phases of the model. Finally, in Sec. VI we conclude and summarize our main results.

II. MODEL

The paradigmatic model of a higher-order topological insulator, the BBH model [8, 9], is described by the Bloch Hamiltonian

$$h_{\text{BBH}}(\mathbf{k}) = \mathbf{d}(\mathbf{k}) \cdot \boldsymbol{\gamma}, \quad (1)$$

where $d_1 = t \sin(k_y a)$, $d_2 = \lambda + t \cos(k_y a)$, $d_3 = t \sin(k_x a)$, $d_4 = \lambda + t \cos(k_x a)$, $\gamma_i = \sigma_2 \otimes s_i$ for $i = 1, 2, 3$, and $\gamma_4 = \sigma_1 \otimes s_0$. The model is defined on a square lattice with a lattice parameter a . The original BBH model can be considered as the collection of spinless fermions on a square lattice with four sublattices, being an extension of the two-dimensional (2D) Su-Schrieffer-Heeger model [68] with a π -flux. Here, we instead interpret σ_i and s_i as Pauli matrices ($\sigma_0 = s_0 = \mathbb{1}_2$) associated with orbital and spin degree of freedom. This Hamiltonian then has spin-orbit coupling between orbital and spin on the same site (terms proportional to λ) and between different sites (terms proportional to t). This choice is motivated for

considering the proximity effect from a conventional superconductor, where the pairing is s -wave (onsite) intra-orbital (proportional to σ_0) spin-singlet (proportional to s_y), which is not possible for spinless fermions. We here further consider the deep topological limit of Eq. (1), by setting $\lambda = 0$. This both generates nontrivial topology in the normal state and removes the need for on-site spin-orbit coupling.

Since it is known that a conventional superconductor with spin-orbit coupling can host topological superconductivity in an in-plane magnetic field [44, 45, 67], we also add an in-plane external magnetic field B_x along x , accounted for by a Zeeman term proportional to s_x . An interesting question then is to investigate the interplay between superconductivity and magnetic field with the intrinsic higher-order topology of the BBH model. The Bogoliubov-de Gennes (BdG) Hamiltonian for this system in the particle-hole basis becomes

$$h_{\text{BdG}}(\mathbf{k}) = \begin{pmatrix} \mathbf{h}(\mathbf{k}) & -i\Delta \\ i\Delta & -\mathbf{h}^*(-\mathbf{k}) \end{pmatrix} = \mathbf{D}(\mathbf{k}) \cdot \mathbf{\Gamma}, \quad (2)$$

where $h(\mathbf{k}) = h_{\text{BBH}}(\mathbf{k}) + B_x \sigma_0 \otimes s_x$ is the total normal-state Hamiltonian. For the second equality we use the vectors $\mathbf{D} = (d_1, d_2, d_3, d_4, B_x, \Delta)$ and $\mathbf{\Gamma}$ to write the Hamiltonian in terms of matrices in the particle-hole, orbital, and spin degrees of freedom. Using τ_i as the Pauli matrices in the particle-hole degrees of freedom, we construct the matrices $\Gamma_i = \tau_3 \otimes \gamma_i$, $\Gamma_4 = \tau_3 \otimes \gamma_4$, $\Gamma_5 = \tau_2 \otimes \sigma_0 \otimes s_2$, and $\Gamma_6 = \tau_3 \otimes \sigma_0 \otimes s_1$. Before investigating the different phases of this system in detail, we next discuss the topological invariants that we use to characterize them.

III. TOPOLOGICAL CHARACTERIZATION

As hinted by the phase diagram in Fig. 1(b), the model Eq. (1) presents a variety of topological phases with a mix of first- and second-order as well as nodal topological phases. In addition, since we are dealing with a spinful topological superconductor, we can have different symmetry-protected boundary states. Therefore, we do a thorough analysis of the topology using three different invariants, which can identify different aspects of the topological phases.

We use the Wannier spectrum [7, 8] to investigate the presence of a non-trivial polarization in the lattice. Since the presence of higher-order topological phases is not completely characterized by the Wannier spectra, we also use a real-space invariant, the entanglement spectrum [60, 69], to verify whether the boundary modes are of higher-order topological origin. Finally, to understand whether these boundary states may be MZMs or ABS, we use the Majorana polarization [65, 66], which indicates how much of a combination of electron and hole a state in a superconductor is. In addition to these invariants, we study the energy spectra using different boundary conditions, the local density of states (LDOS) at zero

frequency, and wavefunctions of the states in the middle of the spectrum to further characterize and verify the phases. Below, we briefly review these topological invariants and explain the signatures of each topological phase.

A. Wannier spectrum

In the modern theory of polarization, the charge polarization is directly related to the Berry phase [7, 70–72] being, therefore, a topological property of a material. However, the direct numerical calculation of these quantities is not so practical due to an overall ill-definition of the phase of wavefunctions [7]. A very convenient alternative is based on the use of Wilson loops [7, 8, 73]. For a 2D system with periodic boundary conditions along x and open boundary conditions along y , the Wilson loop components are defined by [7]¹

$$(W)_{mn}^x = \langle u_m(\pi) | \prod_{k_x}^{\pi \leftarrow -\pi} \mathcal{P}(k_x) | u_n(-\pi) \rangle, \quad (3)$$

where \mathcal{P} is a projector

$$\mathcal{P}(k_x) = \sum_m |u_m(k_x)\rangle \langle u_m(k_x)| \quad (4)$$

over the occupied eigenstates $|u_m(k_x)\rangle$ of the (semi-periodic) Hamiltonian with momentum k_x .

W^x is a unitary matrix which can be associated with the so-called Wannier Hamiltonian H_W^x

$$W^x = e^{i2\pi H_W^x}. \quad (5)$$

The eigenvalues ν^x of H_W^x are the Wannier spectrum of the system with open boundaries along y . A gauge transformation, associated with the change of phases of the wavefunctions, can change ν^x by integer values, making these quantities, in general, defined mod 1. We choose a gauge where ν^x take values between 0 and 1 [7, 8]. The presence of crystalline symmetries imposes some constraints in the Wannier spectrum [7, 8]. For instance, symmetry upon reflection along the x -axis makes ν^x come in $(\nu, 1-\nu)$ pairs [8]. In this way, $\nu^x = 0.5$ are reflection invariant and indicate the presence of boundary modes protected by this symmetry, created by a non-trivial polarization along x [7, 8]. The same holds, mutatis mutandis, to periodic boundary conditions along y with boundaries open along x , obtaining a corresponding ν^y . Thus, when either ν^x or ν^y presents modes at

¹ The Wilson loop, in general, needs to be defined in terms of a reference point \mathbf{k}_i [8] from which the loop is made. However, for the topological invariants considered here, the Wannier spectrum is the same for all reference points, and we thus choose $k_i = -\pi$ for both k_x and k_y .

0.5, or half-quantized modes, we obtain a dipolar phase. For a higher-order topological phase, there are instead half-quantized midgap states in both ν^x and ν^y [8].

An illustrative example is the BBH model in Eq. (1). This model presents reflection symmetry along both x and y , which restricts $\nu^{x/y}$ to appear in pairs. For $|\lambda/t| < 1$, the system is in a second-order, or quadrupolar, topological phase characterized by four corner modes at zero energy, corresponding four 0.5 eigenvalues in both ν^x and ν^y [8]. For reference, for $|\lambda/t| > 1$, the model is in a trivial phase, with no midgap states in both the energy and Wannier spectra [8]. If we further allow t or λ to be different along x and y , we can obtain a phase with polarization just along one of the directions showing first-order topology.

Before moving on, we discuss why we are not using the nested Wilson loop spectrum [8] to characterize the higher-order topological phases. The nested Wilson loop is computed by using the eigenvectors of the Wannier Hamiltonian H_W , Eq. (5), but for fully periodic boundary conditions in the general expression of the Wilson loop in Eq. (3). It is often taken as a clear indicator of higher-order topology, presenting midgap states in its spectrum when there are symmetry-protected higher-order modes [8]. For example, in the BBH model, Eq. (1), the nested Wilson loop is a phase, which is equal to zero in the trivial phase and π in the quadrupolar phase [8]. However, for the nested Wilson loop spectrum to present quantized values, one needs inversion symmetry. But our full system in Eq. (2) breaks mirror symmetry along x : $M_x h_{\text{BdG}}(k_x, k_y)(M_x)^{-1} \neq h_{\text{BdG}}(-k_x, k_y)$ with $M_x = \tau_3 \otimes \sigma_1 \otimes s_3$, while it preserves mirror symmetry along y : $M_y h_{\text{BdG}}(k_x, k_y)(M_y)^{-1} = h_{\text{BdG}}(k_x, -k_y)$ with $M_y = \tau_3 \otimes \sigma_1 \otimes s_1$. Consequently, inversion symmetry, generated by $\mathcal{I} = M_x M_y$, is broken as $\mathcal{I} h_{\text{BdG}}(k_x, k_y) \mathcal{I}^{-1} \neq h_{\text{BdG}}(-k_x, -k_y)$. Therefore, we cannot use the nested Wilson loop as a bulk invariant to diagnose our topological phases. We instead revert to the Wannier spectra along x and y .

B. Entanglement spectrum

Since we cannot use the nested Wilson loop spectrum, but only the Wannier spectrum along x or y , an alternative invariant that can characterize higher-order topological phases is useful. One such invariant has recently turned out to be the entanglement spectrum [60–64, 74, 75]. In the same way that a non-trivial polarization in the lattice can be determined using the Wannier spectrum, it can also be diagnosed by the entanglement spectrum [60–64, 74, 75]. To obtain the entanglement spectrum, we compute the correlation matrix in the occupied state $|\Omega\rangle$

$$C_{\mathbf{r},\tau,\sigma,s;\mathbf{r}',\tau',\sigma',s'} = \langle \Omega | c_{\mathbf{r},\tau,\sigma,s}^\dagger c_{\mathbf{r}',\tau',\sigma',s'} | \Omega \rangle, \quad (6)$$

where $|\Omega\rangle$ represents the (many-body) fermionic ground state and $c_{\mathbf{r},\tau,\sigma,s}^\dagger$ creates a particle ($\tau = 1$) or hole

($\tau = -1$) in orbital σ with spin s at position $\mathbf{r} = (x, y)$. The entanglement spectrum ξ consists of the eigenstates of the correlation function constrained to some finite region in real space. One can intuitively understand the cut(s) needed to create such as finite region as creating artificial boundaries in the system, such that the presence of boundary states may appear in properties of the entanglement spectrum. For instance, for a system with inversion symmetry, the entanglement spectrum of a lattice cut in half displays modes at 0.5 in the topological phase [76], analogously to what happens to the Wannier spectrum. A cut that preserves the symmetries that protect the corner modes can also be used to diagnose the presence of a higher order topological phase [69, 77]. Since these modes are protected by C_4 symmetry, we cut the system in half along both x and y , obtaining a quarter of the original lattice, as indicated by the dashed area in Fig. 1(a). For this cut, the number of ξ modes between 1/4 and 3/4 is equal to the number of C_4 -protected midgap states [69, 77].

C. Majorana polarization

The Majorana polarization P is defined as [65, 66, 78]

$$P_m(x, y) = \sum_{\sigma,s} 2\psi_{x,y,\tau=1,\sigma,s;m} \psi_{x,y,\tau=-1,\sigma,s;m}, \quad (7)$$

where $\psi_{\mathbf{r},\tau=1,\sigma,s;m}$ ($\psi_{\mathbf{r},\tau=-1,\sigma,s;m}$) is the particle (hole) component of the wavefunction of the m -th eigenstate at position $\mathbf{r} = (x, y)$ with orbital σ and spin s . It is a tool to characterize how much particle-hole symmetric a state is. In particular, the comparison between the absolute value of P with the probability density

$$\Psi_m(x, y) = \sum_{\tau,\sigma,s} |\psi_{x,y,\tau,\sigma,s;m}|^2, \quad (8)$$

which measures the spatial properties of the wavefunction, quantifies how much of the wavefunction is particle-hole symmetric. In addition, the phase of P is proportional to the relative phase between the electron and hole components of the wavefunction. As an example, for the MZMs of the paradigmatic 1D Kitaev chain, the Majorana polarization is $P = e^{\pm\pi i}$ [66], with the different signs corresponding to different edges of the system. In contrast, an ABS can present any value of P .

For systems that present only one isolated state per boundary, the Majorana polarization becomes an unambiguous indicator of a MZM. However, if there are many MZMs per boundary, since they are degenerate in energy, one may obtain different values of P for different linear combinations of the states at zero energy. Thus, even if we numerically find a high value of the Majorana polarization compared to the probability density, it can be unclear whether two such putative MZMs can actually recombine into a complex fermion. For such recombination to not occur, different spin and orbital degrees of

freedom generally have to be in play. Such ambiguousness is the case for some topological phases in our system and we can thus not use P as a unique indicator in these cases. Nevertheless, we still investigate the midgap states in terms of the Majorana polarization to provide an additional tool whenever it is distinctive. Since we always obtain a real P , we use only its real value to check the sign across the lattice.

D. Spectral characterization

In addition to the topological invariants discussed above, it is useful to consider how the energy spectrum and the wavefunctions of the system behave in every phase. Symmetry-protected topological states appear at zero energy at the boundaries for a gapped or nodal bulk. Since, in our case, we have surface modes localized both on the edges and corners of the lattice, we extract the energy spectra for different boundary conditions. For the bulk spectrum we apply fully periodic boundary conditions and generally sample the Brillouin zone taking paths connecting the high-symmetry points of the square lattice $\Gamma = (0, 0)$, $X = (\pi/a, 0)$, $Y = (0, \pi/a)$, and $M = (\pi/a, \pi/a)$. For edge or corner states we apply open boundary conditions in the appropriate directions. For the midgap states we plot both the wavefunction $\Psi_m(x, y)$, to verify in which part of the boundary these states are localized, and the Majorana polarization to verify whether these states are MZMs or not. Since the Hamiltonian is particle-hole symmetric, there is a correspondence between states with infinitesimally small positive energy ($\epsilon = 0^+$) and those with infinitesimally small negative energy ($\epsilon = 0^-$). Therefore, when showing the localization and Majorana polarization properties of the midgap modes of the HOTSC and hybrid phases, we, for convenience, focus on the states with energy $\epsilon = 0^-$. To obtain complete information on the localization of all low-lying states in the system, we also show the local density of states (LDOS) at zero frequency $\omega = 0$.

IV. TOPOLOGICAL PHASES

In this section we present our main analysis of the topological phases of the model in Eq. (1) using the topological invariants discussed in Sect. III. We focus on the deep topological limit of the BBH model, setting $\lambda = 0$ for simplicity, which allow us to obtain analytical expressions of the phase boundaries, but we remark that the topological phases are present for $|\lambda/t| < 1$. We refer to Appendix A for results on finite λ . For $\lambda = 0$, the topological phase diagram is displayed in Fig. 1(b). Here, we start by detailing how we obtain the phase boundaries, followed by a detailed description of each of the phases.

A. Phase boundaries

A quantum phase transition is accompanied by the closing of the gap of the system [79]. Therefore, the topological phase boundaries are obtained by considering the energy gap, δ between the highest valence band and the lowest conduction band around zero energy. In Fig. 2 we plot δ as a function of the superconducting order parameter Δ and magnetic field B_x for different boundary conditions. Starting with fully periodic boundary conditions in Fig. 2(a), we obtain that the bulk gap closes along several different lines. For $B_x = \sqrt{2t^2 + \Delta(\Delta - 2t)}$ (magenta dashed line) the bulk spectrum closes at momenta $(k_x, k_y) = (0, \pi/2)$ and $(\pi, \pi/2)$ and for $\Delta = \sqrt{2t^2 + B_x(B_x - 2t)}$ (yellow dashed line) it closes at momentum $(\pi/2, \pi/2)$. These two lines separates the nodal flat bands phase (blue region in Fig. 1(b)) from the nodeless flat bands phase (red region in Fig. 1(b)) and hybrid phase. Further, the bulk spectrum also closes at $B_x = \sqrt{2t^2 + \Delta(\Delta + 2t)}$ (green dashed line) at momentum $(k_x, k_y) = (\pi, \pi/2)$ and at $\Delta = \sqrt{2t^2 + B_x(B_x + 2t)}$ (cyan dashed line) at momentum $(\pi/2, \pi/2)$, which separates the trivial phase from the nodal flat band phase. These results also establish that the HOTSC (yellow in Fig. 1(b)), hybrid (green), trivial (white), and nodeless flat band (red) phases are all fully gapped in the bulk.

To complement the results for fully periodic boundary conditions, we also analyze how the gap closes for open boundary conditions along y in Fig. 2(b) and along x in Fig. 2(c). This analysis of different boundary conditions brings three important pieces of information. First, we notice that there is a new gap-closing line at $\Delta = \sqrt{2}t - B_x$ (white dashed line), which indicates the phase boundary between the HOTSC and hybrid phases in Fig. 1(b). This line just appears for x -open boundary conditions, see Fig. 2(c), illustrating how the gap only closes along the y -direction. Already this result points to the higher order topology of its neighboring phases. Second, we notice that the nodal flat bands phase (blue in Fig 1(b)) actually seemingly hosts a small but finite gap, seen as red arcs in Figs. 2(a,c), but it does become completely gapless in Fig. 2(b). In fact, for all values of B_x and Δ in this phase, the gap closes at $k_y = \pi/2$ and different k_x . Therefore, the spectrum is actually gapless in all three figures and the red arcs are just finite-size effects due to a necessarily finite k_x -point sampling in Figs. 2(a,c). This verifies that the nodal flat bands phase is a bulk nodal phase. Finally, we find that one of the bulk gapped regions, the nodeless flat band phase (red in Fig. 1(b)) is also gapped for x -open boundary conditions but notably not for y -open boundary conditions, as seen in Fig. 2(b). This indicates zero-energy states localized to edges along the x -direction.

In the next subsections, we detail the properties of each of the non-trivial topological phases, while the trivial phase is discussed in Appendix B. We characterize the general properties considering both the energy spectra

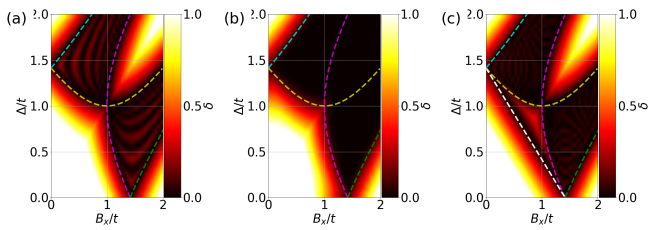


FIG. 2. Energy gap δ between the highest valence band and lowest conduction band around zero energy, derived from Eq. (2), as a function of superconducting pair amplitude Δ/t and in-plane magnetic field B_x/t for (a) fully-periodic, (b) x -periodic (open in y) and (c) y -periodic (open in x) boundary conditions. Parameters used: $\lambda = 0$, system size 32 unit cells in each direction.

extracted above and the topological invariants discussed in Sec. III, for representative values of B_x and Δ in all phases.

B. HOTSC phase

For small B_x and Δ , we find a phase that we call the HOTSC phase, indicated by the yellow region in Fig. 1(b). The main features of this phase are summarized in Fig. 3. First, considering the energy ϵ spectrum for fully periodic in Fig. 3(a), x -periodic in Fig. 3(b), y -periodic in Fig. 3(c), and fully open in Fig. 3(d) boundary conditions, we realize that the bulk of the system is gapped, while there are eight states at zero energy present only for fully open boundary conditions, Fig. 3(d). The system is thus gapped under x - or y -periodic boundary conditions in this phase. Plotting the LDOS at zero frequency/energy in Fig. 3(e), we see that these states are corner states, explaining why they appear just for open boundary conditions. To further understand the properties of these zero energy modes, we examine the Wannier spectrum ν along both x in Fig. 3(f) and along y in Fig. 3(g). The half-integer values of both $\nu_{x,y}$ indicate the higher-order character of this phase. We note, however, that within increasing value of Δ and B , but still in the HOTSC phase, the midgap values of ν^x deviate significantly from 0.5 due to the breaking of mirror symmetry along x . Nevertheless, we still have robust corner modes with properties similar to the ones discussed below. The higher-order aspect is corroborated by the entanglement spectrum ξ in Fig. 3(h), which shows distinct isolated half-quantized modes inside the midgap region.

Finding a total of eight corner modes, two at each corner is expected considering the BBH model at $B_x = \Delta = 0$ [38, 80]. Due to the finite Δ , however, the corner modes are now a combination of particles and holes as they are Bogoliubov quasiparticles in a superconductor. In Figs. 4(a-d) and (e-h) we analyze, respectively, the zero-energy Bogoliubov quasiparticles by plotting the wavefunction Ψ from in Eq. (8) and Majorana polarization P

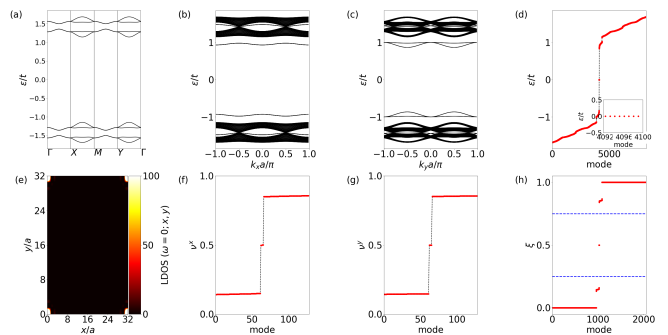


FIG. 3. Main features of the HOTSC phase. Energy spectrum ϵ for fully periodic (a), x -periodic (b), y -periodic (c), and open (d) boundary conditions. Inset in (d) a zoom-in on the modes in the middle of the spectrum with energy $\epsilon = 0$. LDOS at zero energy (e). Wannier spectrum along x (f) and y (g). Entanglement spectrum ξ (h). Blue dashed lines mark the values of 0.25 (1/4) and 0.75 (3/4). Parameters used: $B_x = 0.2t$, $\Delta = 0.1t$, $\lambda = 0$, system size 32 unit cells for directions with open boundary conditions and 100 k -points.

from Eq. (7) of the four states at zero (negative) energy. As seen, these modes are fully localized at the corners, as shown in both Ψ and P . Moreover, since P is much smaller than Ψ , not being even visible in this scale, and since there are two states per corner, we designate these states as ABSs.

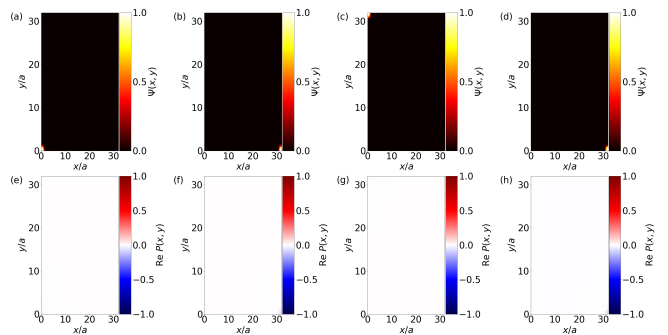


FIG. 4. HOTSC boundary states features. (a-d) Wavefunction probability density Ψ and (e-h) Majorana polarization P for the four states with $\epsilon = 0^-$ in the HOTSC phase. Parameters same as in Fig. 3.

C. Hybrid phase

For increasing values of Δ and B_x , the system enters into the hybrid phase, green region in Fig. 1(b). While present only in a narrow region of the phase diagram, it displays interesting features.

We analyze the general properties of this phase in Fig. 5. We find that it has energy spectrum similar to the HOTSC phase: both the bulk, Fig. 5(a), and the edges, Figs. 5(b,c), are gapped while there are eight midgap states at zero energy for open boundary condi-

tions, Fig. 5(d). These midgap states are still located at the corners, as shown in the LDOS at zero energy, Fig. 5(e). However, when inspecting the Wannier spectrum, Figs. 5(f,g), we see that ν^y is half-quantized, while ν^x exhibits a gap around 0.5. Further, the entanglement spectrum in Fig. 5(h) shows a continuous array of midgap eigenvalues that are present symmetrically around $\xi = 0.5$. Therefore, this hybrid-order phase can be considered topologically distinct from the previous HOTSC phase. We remark that since ν^x is not quantized for larger values of Δ and B in the HOTSC phase, the topological phase transition between the two phases is due to the change of localization of some of the zero energy states, as shown below.

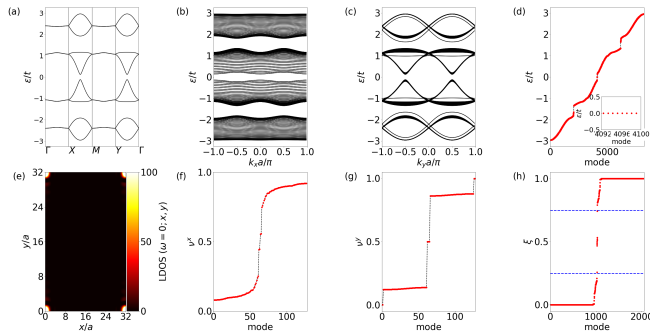


FIG. 5. Main features of the hybrid phase. Same panels as in Fig. 3. Parameters used: $B_x = 0.9t$, $\Delta = 0.8t$, $\lambda = 0$, system size 32 unit cells for directions with open boundary conditions and 100 k -points.

By going back to Figs. 2(a,b), we see that there is no change in the energy gap from the phases HOTSC and hybrid for systems with periodic conditions along x , indicating that the change from the phase HOTSC to the hybrid phase is due to properties related to the I and III edges, which are along the y -direction. As a consequence, only when periodic boundary conditions are applied along the y -direction, the gap closing, indicating a topological phase transition, is noticed between the HOTSC and hybrid phases.

Continuing to analyze the wavefunctions in Figs. 6(a-d) and Majorana polarization in Figs. 6(e-h), we find that half, Figs. 6(a,b), of the zero-energy states with $\epsilon = 0^-$ have a significant weight not just at the corners but also partially along the y -direction, even better visualized in the Majorana polarization, Figs. 6(e,f), while the other half of the $\epsilon = 0^-$ states, Figs. 6(c,d), are still localized at the corners of the lattice, as in the HOTSC phase. As a consequence, we find a combination of corner modes, as appropriate for a second-order topological phase and clearly a remnant of the HOTSC second-order phase, and more extended edge-localized modes. The latter is also expected for a first-order topological phase, but here we note that we only have a finite number of modes localized at the edge, four to be precise, which do not grow with system size, and thus the modes are not representable of a standard first-order topological phase. Instead, the

edge modes are those of a dipolar phase [12, 81], which can be seen as created as the edge of a single 1D system extending in the y -direction. Due to this combination of boundary modes, we name this a hybrid-order phase, being an interesting mix of different topologies. However, note that our use of the word hybrid should not be confused with the situation where more standard first- and second-order phases are appearing at the same time, also called a hybrid phase [82–86]. Here, the hybrid phase is instead a standard second-order phase appearing jointly with a dipolar phase.

Moreover, with all eight zero-energy modes now spatially distinct and also presenting similar values for Ψ and $|P|$ as seen in Fig. 6, we find them to be fully particle-hole symmetric. Therefore, the increase of Δ and B_x moving from the HOTSC to the hybrid phase turn the surviving four corner modes in the HOTSC phase corner-localized, single, MZMs and the other four into edge-extended MZMs.

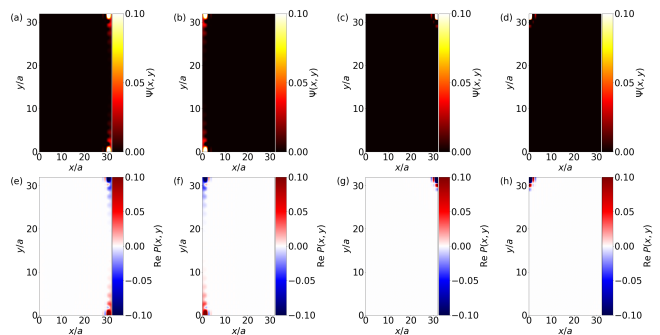


FIG. 6. Hybrid phase boundary states features. Same panels as in Fig. 4 for the four states with $\epsilon = 0^-$ in the hybrid phase. Parameters same as in Fig. 5.

D. Nodal flat bands phase

Increasing either Δ or B_x , we arrive at the nodal flat band phase, represented in blue in Fig. 1(b). This phase is characterized by bulk nodal points, *i.e.* there exists momenta where the bulk energy gap (superconducting gap) closes. Between these bulk nodal points, we find flat bands that appear localized to the boundaries of the system. We investigate the general properties of this phase in Fig. 7. Considering the energy dispersion along the high-symmetry points in Fig. 7(a), the bulk of the system seems to be gapped, in contradiction to Fig. 2(a). However, analyzing the energy spectrum for the system with open boundary conditions along y , in Fig. 7(b) and x in Fig. 7(c), we understand that this happens because the bulk gap is only zero at specific points $k_x a \neq 0, \pi$. The bulk gap vanishes away from the high-symmetry line and that is why gap-closing is not visible in Fig. 7(a). Additionally, there exist zero-energy flat bands along k_x , which connect these bulk nodal points, while all bands are dispersive along k_y . This suggests that the flat bands

are boundary states localized along the edges II and IV in Fig. 1(a). These flat bands cause the energy spectrum with fully open boundary conditions in Fig. 7(d) to host a macroscopic degeneracy at zero energy, as shown in the inset of Fig. 7(d).

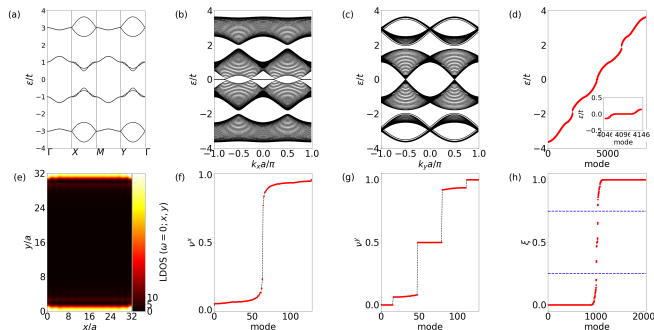


FIG. 7. Main features of the nodal flat band phase. Same panels as in Fig. 3. Parameters used: $B_x = 1.5t$, $\Delta = 0.9t$, $\lambda = 0$, system size 32 unit cells for directions with open boundary conditions and 100 k -points.

Further evidence that the zero-energy states are localized along the II and IV edges is shown in the LDOS at zero frequency in Fig. 7(e), which shows weight just at these edges. This indicates that these are the boundary states of a first-order topological phase, also since the absence of corner modes clearly discards these phase as any higher-order phase. We find this fully consistent with the topological invariants: an absence of midgap modes in ν^x in Fig. 7(f), while a number of 0.5 modes in ν^y appears in Fig. 7(g). We further find that the number of zero-energy states and 0.5 modes in ν^y scales with the number of unit cells along x , which further corroborates that this is an edge phenomenon along the x -direction. Here ν^y is thus an invariant that characterizes the presence of these zero-energy states, which are related by a bulk-boundary correspondence to the nodes in the bulk [2, 55, 57]. Another indication that this is not a second-order phase is the entanglement spectrum in Fig. 7, which does not show sharply quantized modes at 0.5. We instead find a discontinuous array of mid-gap eigenvalues symmetrically placed around 0.5.

To better understand the overall properties of the zero-energy flat bands occurring between the bulk nodal points, we plot in Fig. 8 the wavefunction Ψ in Figs. 8 (a-d) and the corresponding Majorana polarization P in Figs. 8 (e-h), for four of the zero-energy modes. It is here most convenient to consider a system with open boundary conditions along y and periodic boundary conditions along x (corresponding to the spectrum of Fig. 7(b)) for $k_x = 0$. After diagonalizing we then have a wavefunction $\psi(k_x = 0, y)$ and to obtain a complete real space wavefunction, we multiply

$$\psi_{k_x=0}(x, y) = 1/\sqrt{L} \exp(ik_x x) \tilde{\psi}(k_x = 0, y).$$

This is the wavefunction we use to compute the probability density and Majorana polarization in Figs. 8 and

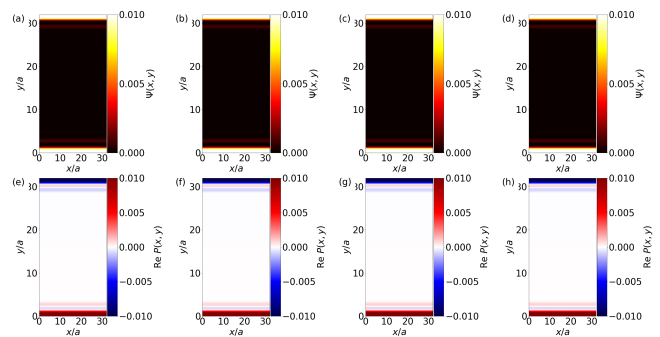


FIG. 8. Nodal flat band phase boundary states features. Same panels as in Fig. 4 for the four states for $\epsilon = 0$ for $k_x = 0$ in the nodal flat band phase, using a partial Fourier transform, as explained in the main text. Parameters same as in Fig. 7.

we find four-zero energy modes for $k_x = 0$. We also find four-zero energy modes for each other value of momentum. The Majorana polarization P has the same maximum value as the wavefunction probability Ψ and also changes sign between the two edges for all modes, indicating that they resemble that of MZMs. Still, since there is a degeneracy of two zero-energy modes per edge per momentum in this phase, we cannot for sure classify these states as MZMs without considering if a linear combination of them cannot recombine into complex fermionic modes. However, since these modes present a strong Majorana polarization and we have two possible particle-hole symmetric pairs that we can build with spin and orbital degrees of freedom, we choose to still call these states flat band MZMs. We note that these flat band MZMs are extended along the edges, and their number increases with system size, in contrast to the MZMs obtained for the hybrid phase that are always just one per edge and one per corner, as discussed in Sec. IV C.

E. Nodeless flat bands phase

Finally, moving closer to the diagonal of the phase diagram, with $\Delta/t \approx B_x/t > 1$, we find the nodeless flat band phase in red in Fig. 1(b). For this phase, the bulk system is gapped, as seen in Fig. 9(a), as is the semi-infinite spectrum with the open boundary along x , illustrated in Fig. 9(c). In Fig. 9(b), we instead find zero-energy flat bands spanning the whole Brillouin zone along k_x . Fully open boundary conditions also generate zero-energy mid-gap states in Fig. 9(d). Plotting the zero-energy LDOS we find that these flat bands are localized on the II and IV edges in Fig. 9(e). Further, although ν^x is completely gapped in Fig. 9(f), ν^y in Fig. 9(g) has a microscopic number of 0.5 modes, which grows with the number of unit cells along x . This ν^y profile confirms that the zero-energy states are an edge phenomenon along the x -direction. Finally, the entanglement spectrum in Fig. 9(h) shows a discontinuous array of mid-gap eigen-

values around 0.5 while they gather more closely to 0.5. This is qualitatively similar to the nodal flat band case, however, the discontinuous profile is more asymmetric around 0.5 in this case compared to the previous case.

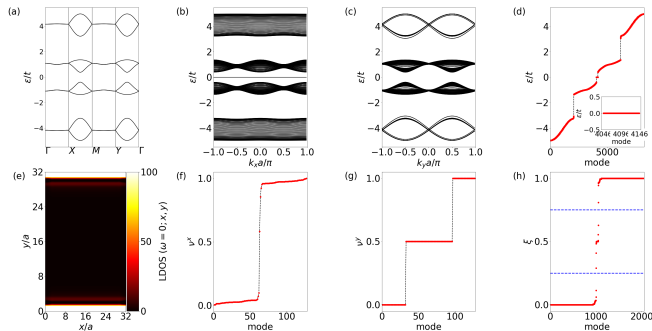


FIG. 9. Main features of the phase with nodeless flat bands. Same panels as in Fig. 3. Parameters used: $B_x = 1.8t$, $\Delta = 2t$, $\lambda = 0$, system size 32 unit cells for directions with open boundary conditions and 100 k -points.

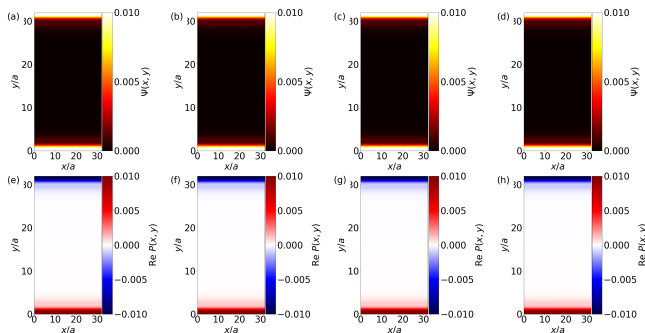


FIG. 10. Nodeless flat band boundary states features Same panels as in Fig. 4 for the four states with $\epsilon = 0$ for $k_x = 0$ on the nodeless flat band phase, using a partial Fourier transform, as explained in the main text. Parameters same as in Fig. 9.

To investigate the spatial properties of the states at zero energy in this phase, shown in Fig. 10, we focus on the semi-periodic system with $k_x = 0$ (corresponding to the spectrum of Fig. 9 (b)) as done for the nodal phase. Although the modes present a similar spatial profile, we remark that these flat bands are present without corresponding nodal points in the bulk. As such, they are a very different kind of surface state compared to those of the nodal flat band phase. We currently do not know how they can be fully classified in terms of symmetry-protected topological phases. Nevertheless, they are still topologically protected by symmetry since the number of states at zero energy is determined by the number of 0.5 states in ν^y , which is a topological property. Finally, we note that these flat bands states again present a Majorana polarization P of the same amplitude as the of the wavefunction density Ψ , Figs. 10(e-h), which makes them designated as flat band MZMs in a similar way to in the nodal flat band case.

V. ANALYTICAL RESULTS

After having described in detail the properties of all the different topological phases numerically, we also present some results feasible to achieve analytically in order to enhance the overall understanding. While a complete analytical treatment at present seems not possible, we can still obtain selective analytical results. Here, we first present analytical calculations supporting the existence of a nodal phase despite an s -wave superconducting order parameter. For this purpose, we define a dual Hamiltonian. In addition to a dual Hamiltonian, we also extract a low-energy Hamiltonian and are able to show analytically that corner states exist in its regime of validity.

A. Nodal superconductivity

One of the phases, the nodal flat band phase, depicted in blue in Fig. 1(b) and discussed in detail in Sec. IV D, hosts bulk nodes. This is despite the model only containing on-site, or in k -space isotropic s -wave, pairing, which are usually associated with a fully gap, while nodes are usually thought of as requiring a k -dependent order parameter. The presence of nodes in the nodal flat band phase can be understood as a consequence of the spin-orbit coupling in the normal state Hamiltonian, as such terms can induce an effective momentum-dependent pairing. The equivalence between the spin-orbit coupling and nodal superconductivity can be seen explicitly by performing the unitary transformation of the Hamiltonian of Eq. (2) (for $\lambda = 0$):

$$h_D(\mathbf{k}) = U h_{\text{BdG}}(\mathbf{k}) U^\dagger; \quad U = \begin{pmatrix} \sigma_0 \otimes s_0 & i\sigma_2 \otimes s_2 \\ i\sigma_2 \otimes s_2 & \sigma_0 \otimes s_0 \end{pmatrix}, \quad (9)$$

where we obtain a dual Hamiltonian h_D , following the nomenclature of Ref. [67], with the form

$$h_D(\mathbf{k}) = \tau_1 [-t \sin(k_y a) \sigma_0 s_3 - t \cos(k_x a) \sigma_0 s_1 + B_x \sigma_2 s_3] + \Delta \tau_3 \sigma_1 s_0 - t \cos(k_y) \tau_0 \sigma_2 s_2, \quad (10)$$

where we omit the outer product symbol \otimes for convenience.

In the dual Hamiltonian in Eq. (10), the superconducting pairing appears in multiple terms. There is pairing with p -wave intra-orbital spin-triplet pairing symmetry given by $-t \sin(k_y a) \tau_1 \otimes \sigma_0 \otimes s_3$, with extended s -wave intra-orbital spin-singlet symmetry given by $-t \cos(k_x a) \tau_1 \otimes \sigma_0 \otimes s_1$, and with s -wave odd-interorbital spin-triplet symmetry given by $B_x \tau_1 \otimes \sigma_2 \otimes s_3$. The first two terms always present nodes at some k_x and k_y coordinates and result in the nodal profile of the superconducting order parameter. If such nodes in the superconducting order parameter also overlap with the normal-state Fermi surface, then the system will have a nodal energy gap. In the presence of the third term $B_x \neq 0$, the nodal structure caused by the first two terms

can still be retained with nodes then appearing at different values of k_x and k_y in appropriate parameter regimes. This qualitatively explains why a nodal state at all can be possible and also shows how it is intricately linked to the Δ and B_x parameters. We further note that in the pairing terms, the dependence on k_x comes from a hopping term $\cos(k_x a)$, while $\sin(k_y a)$ appears due to the spin-orbit coupling of the normal state. This difference, together with the fact that the magnetic field is applied along x , explains the asymmetry seen in the properties of the system with periodic boundary conditions along x or y . Finally, the existence of a p -wave term is also an underlying reason for the existence of MZMs in several of the different phases.

B. Corner states

In addition to the dual Hamiltonian, we can also analytically study a low-energy continuum Hamiltonian. This is a technique commonly used to connect the presence of localized boundary states with a non-trivial mass profile, as first constructed by Jackiw and Rebbi[87], and where the mass profile tells us some properties of the topological phase. For instance, for a higher-order topological system, the mass profile needs to change sign between two adjacent edges [8, 35], with the corner in between hosting the localized boundary state. To obtain the most simple low-energy Hamiltonian, we keep just terms that are first-order in momentum in h_{BdG} in Eq. (1) and obtain

$$h_{\Gamma}(\mathbf{k}) = tk_y a \Gamma_1 + t \Gamma_2 + tk_x a \Gamma_3 + t \Gamma_4 + \Delta \Gamma_5 + B_x \Gamma_6. \quad (11)$$

Here $\mathbf{k} = (k_x, k_y)$ represents the continuum momentum in relation to the Γ point.

We can obtain the low-energy descriptions of any corner states of h_{Γ} by substituting $k_{x/y} \rightarrow -i\partial_{x/y}$ and looking for localized solutions. The complete calculation is reported in detail in Appendix C, and here we comment on the results. Considering appropriate boundary conditions, the solutions of h_{Γ} localized on the I and III edges are

$$\psi^{1/\text{III}}(x, y) = \sum_{l, m = \pm 1} c_{l, m} \mathcal{N}_x e^{\mp \sqrt{2} \frac{x}{a}} e^{ik_y y} \chi_{l, m}^{1/\text{III}}, \quad (12)$$

where \mathcal{N}_x is a normalization factor, $\sum |c_{l, m}|^2 = 1$, and the spinors $\chi_{l, m}^{1/\text{III}}$ are given by

$$\chi_{l, m}^{\text{I}} = |l, m\rangle \frac{|s = 1\rangle + (m - \sqrt{2}) |s = -1\rangle}{\sqrt{4 - 2m\sqrt{2}}}, \quad (13)$$

and

$$\chi_{l, m}^{\text{III}} = |l, m\rangle \frac{|s = 1\rangle - (m + \sqrt{2}) |s = -1\rangle}{\sqrt{4 + 2m\sqrt{2}}}, \quad (14)$$

where $l = \pm 1$, $m = \pm 1$, and $s = \pm 1$ are eigenvalues of τ_3 , σ_3 and s_3 , respectively. We further obtain the edge

Hamiltonians by projecting the low-energy Hamiltonian in the subspace of Eqs. (13) and (14), yielding

$$h^{\text{I}}(k_y) = -tk_y a \tau_3 \otimes \sigma_2 - \frac{B_x}{\sqrt{2}} \tau_3 \otimes \sigma_0, \quad (15)$$

$$h^{\text{III}}(k_y) = -tk_y a \tau_3 \otimes \sigma_2 - \frac{B_x}{\sqrt{2}} \tau_3 \otimes \sigma_0. \quad (16)$$

These are Dirac-like Hamiltonians with a mass term proportional to B_x . Note that both solutions in Eqs. (13) and (14) are polarized in the effective particle-hole space, represented by τ_3 , while they are a combination of different spin states with the effective spin degrees of freedom represented by σ_3 . Note here that since the edge Hamiltonians are projected Hamiltonians, the original notion of particle-hole or spin is replaced by their effective notions. Turning to the localized solutions on the II and IV edges, we obtain similarly as on the other edges

$$\psi^{\text{II/IV}}(x, y) = \sum_{l, m = \pm 1} \tilde{c}_{l, m} \mathcal{N}_y e^{ik_x x} e^{\mp \sqrt{2} \frac{y}{a}} \chi_{l, m}^{\text{II/IV}}, \quad (17)$$

where \mathcal{N}_y is a normalization factor, we have $\sum |\tilde{c}_{l, m}|^2 = 1$, and the spinors $\chi_{l, m}^{\text{II/IV}}$ are given by

$$\chi_{l, m}^{\text{II}} = |l, m\rangle \frac{|s = 1\rangle - m(1 + \sqrt{2}) |s = -1\rangle}{\sqrt{4 + 2\sqrt{2}}}, \quad (18)$$

and

$$\chi_{l, m}^{\text{IV}} = |l, m\rangle \frac{|s = 1\rangle + m(1 - \sqrt{2}) |s = -1\rangle}{\sqrt{4 + 2\sqrt{2}}}, \quad (19)$$

where again $l = \pm 1$, $m = \pm 1$, and $s = \pm 1$ are eigenvalues of τ_3 , σ_3 and s_3 , respectively.

Again projecting on the solutions of Eqs. (18) and (19), we obtain the effective Dirac Hamiltonians

$$h^{\text{II}}(k_x) = tk_x a \tau_3 \otimes \sigma_2 - \frac{1}{\sqrt{2}} B_x \tau_3 \otimes \sigma_3, \quad (20)$$

$$h^{\text{IV}}(k_x) = tk_x a \tau_3 \otimes \sigma_2 - \frac{1}{\sqrt{2}} B_x \tau_3 \otimes \sigma_3. \quad (21)$$

Having extracted all four edge Hamiltonians, Eqs. (15), (16), (20), and (21), we note that all four edges have a mass term proportional to B_x . On the I and III edges, it is proportional to $\tau_3 \otimes \sigma_0$, while on the II and IV edges it is proportional to $\tau_3 \otimes \sigma_3$. Since eigenvalues of σ_0 and σ_3 can be different in terms of their signs, there exists a sign change in the mass term for adjacent edges. For a given subspace defined by τ_3 , we can hence obtain a positive mass B_x on edges II and IV, while having a negative mass $-B_x$ on edges I and III, when σ_3 is projected on the effective spin-down states. This leads to the formation of corner modes between adjacent edges. On the other hand, for the effective spin-up projections, all the edges have negative mass terms given by $-B_x$, and hence corner modes are not expected to appear. The

effective spin-polarized nature of the corner modes can be attributed to the sign-polarized Majorana polarization for a given corner mode. This analysis qualitatively explains the emergence of corner states for our model, Eq. (2), in both the HOTSC and hybrid phases.

VI. CONCLUSIONS

In this work, we investigate the topological phases of an orbital BBH model proximitized to a conventional spin-singlet s -wave superconductor and in the presence of an in-plane magnetic field. The interpretation of the BBH model in terms of orbital and spin degrees of freedom makes the superconducting pairing have a matrix structure not present in the original dimerized lattice of the BBH model and allows for an intriguingly rich topological phase diagram, despite using only a conventional superconductor. We map out the phase diagram by considering different boundary conditions and investigate the topology of the individual phases by calculating both the Wannier and entanglement spectra, as well as the Majorana polarization.

At weak superconducting pairing Δ and magnetic field B_x , we find a HOTSC phase (yellow in Fig. 1(b)) with eight zero-energy corner modes. This phase can be seen as analogous to the standard second-order topological phase in the BBH model but now with particle and hole degrees of freedom since the system is superconducting. Beyond this expected HOTSC phase, we also find several other, unexpected, topological phases. First, an unusual hybrid phase (green in Fig. 1(b)) presents an atypical mix between the second-order and a first-order topological phase. Here four zero-energy corner states from the HOTSC phase are preserved, while a dipolar phase contributes another four zero-energy edge states, all experiencing MZM character. Notably, the number of edge states does not grow with system size in the hybrid phase despite its mixed-order character. Second, two additional first-order phases present symmetry-protected zero-energy flat bands on opposite edges, with either nodal or nodeless bulk dispersion. The nodal flat bands phase (blue in Fig. 1(b)) presents flat bands MZMs that are straightforwardly connected by a bulk-boundary correspondence to the bulk nodes. However, in the nodeless flat bands phase (red in Fig. 1(b)) the bulk remains fully gapped and the flat bands MZMs now spans the whole edge Brillouin zone and are protected by a quantized Wannier spectrum. These results not only establish the rich phase diagram of a superconducting BBH model, but also demonstrate the existence of both unusual hybrid mixing of topological phases and nodeless flat bands.

Note added: During the final preparation of this work we became aware of the recent work Ref. [88], where zero-energy flat bands are also found to appear as topological boundary states in a nodeless superconductor. However, in that case the flat band is protected by a bulk invariant in 3D. Our flat band instead appears in a 2D system and

is protected by a 1D edge invariant. It remains to be studied if deeper similarities between the two exist.

ACKNOWLEDGMENTS

We are grateful for discussions with A. K. Ghosh, A. Saha, S. Mondal, B. Roy, V. Juricic, O. A. Awoga, D. Chakraborty, and A. Bhattacharya. We acknowledge financial support from the Knut and Alice Wallenberg Foundation. Part of the simulations were enabled by resources provided by the National Academic Infrastructure for Supercomputing in Sweden (NAISS) and the Swedish National Infrastructure for Computing (SNIC) at UPPMAX, partially funded by the Swedish Research Council through grant agreements no. 2022-06725 and no. 2018-05973.

Appendix A: Finite λ

In the main text, we focus on the properties of Eq. (2) for $\lambda = 0$. Here, we discuss the effect of having a finite λ in the phases discussed in the main text. For large $\lambda > t$, the system is just a trivial superconductor. For smaller but finite λ , the phase boundaries of the system change considerably but the topological phases largely persist. In Fig. 11 we set $\lambda = 0.5t$ and we repeat the plot of the energy gap δ as a function of B_x and Δ from Fig. 2. We still retain the phases discussed in the main text, although the phase boundaries change considerably and now cannot be computed analytically. In addition, we obtain a new phase, which we call the dipolar phase, described next.

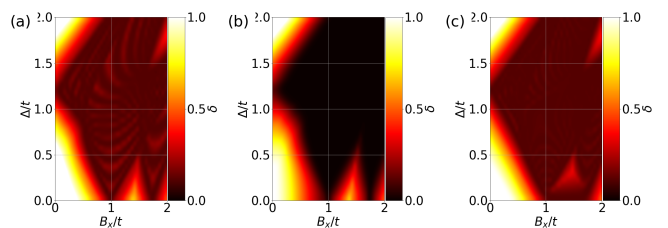


FIG. 11. Energy gap δ derived from Eq. (2) as a function of Δ/t and B_x/t for (a) fully-periodic, (b) x -periodic (open in y) and (c) y -periodic (open in x) boundary conditions. Parameters used: $\lambda = 0.5t$, system size 32 unit cells in each direction.

1. Dipolar phase

With λ finite, but smaller than t , we find a different kind of first-order topological phase appearing for higher values of either Δ and B_x , when one is much larger than the other. This phase, as shown in Fig. 12(a-d), has a gapped bulk but with some localized midgap states on

the I and III edges, as shown in the zero-energy LDOS in Fig. 12(e). The ν^x invariant along x is not quantized, see Fig. 12(f), while the ν^y presents two half-quantized values, see Fig. 12(g), indicating that there are four symmetry-protected modes. The entanglement spectrum shows a symmetric discontinuous distribution of eigenvalues excluding 0.5 within the mid gap region as depicted in Fig. 12(h).

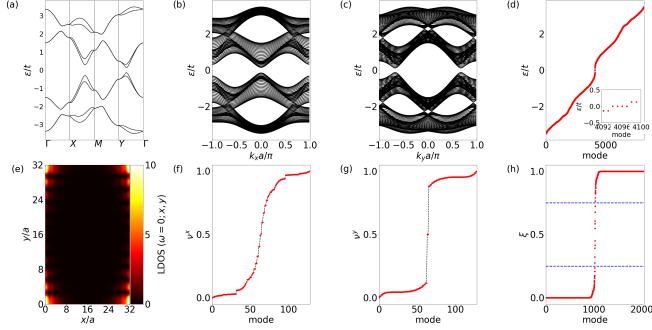


FIG. 12. Main features of the dipolar phase. Same panels as in Fig. 3. Parameters used: $B_x = 1.5t$, $\Delta = 0.2t$, $\lambda = 0.5$, system size 32 unit cells for directions with open boundary conditions and 100 k -points. I am not sure whether we are interchanging between ν_x and ν_y .

In Fig. 13, we plot the wavefunction probability Ψ in Fig. 13(a-d) and the Majorana polarization P in Fig. 13(e-h), for the four states with negative energy in the inset of Fig. 12(d), just as for all other phases investigated earlier. The states with finite energy, seen Figs. 13(a,b), are identically localized on the I and III edges, respectively, and their P oscillate around zero along the edge for both edges, see Figs. 13(e,f). In contrast, the states with zero energies are localized more in the corner of these edges, see Figs. 13(c,d), and P change sign only once along the edges on the lattice, see Figs. 13(g,h). These zero-energy states, therefore, resemble that of the edge states in the hybrid phase discussed in Section IV C, while the corner states of the hybrid phase are notably absent here. Due to the similarity with the dipolar edge states in the hybrid phase, we call this a dipolar phase. We note that the P of the zero-energy boundary states appropriately also resembles an electric dipole.

Appendix B: Trivial phase

For high values of only Δ or B_x , we find a topologically trivial phase. For $\lambda = 0$, this occurs for $\Delta > \sqrt{2t^2 + B_x(2t + B_x)}$ or $\Delta < -t + \sqrt{B_x^2 - t^2}$, corresponding to the white region in Fig. 1(b). Although this phase is topologically trivial, for completeness, we display the main features of this phase in Fig. 14. The system is gapped for all boundary conditions, see Figs. 14(a-d), which is supported by the LDOS at zero frequency, see

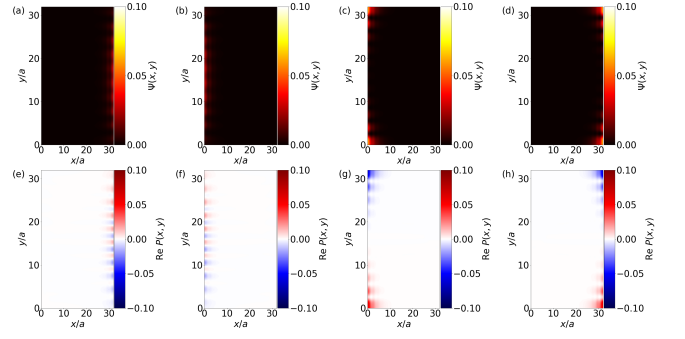


FIG. 13. Dipolar phase boundary states features. Same panels as Fig. 4 for the four states with smallest (negative energy), but where only the last two states (c,d,g,h) have energy $\epsilon = 0^-$, in the dipolar phase. Parameters same as in Fig. 12.

Fig 14(e), which shows no occupation. Further, all topological invariants indicate a trivial system, see Figs. 14(f-h).

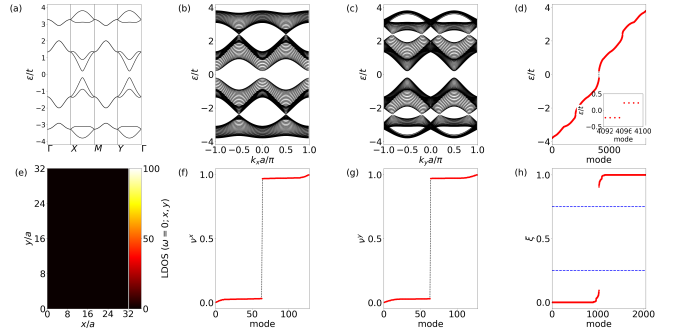


FIG. 14. Main features of the trivial phase. Same panels as in Fig. 3. Parameters used: $B_x = 2t$, $\Delta = 0.5t$, $\lambda = 0$, system size 32 unit cells for directions with open boundary conditions and 100 k -points.

Appendix C: Derivation of edge Hamiltonians

Here we provide the detailed derivation of the edge Hamiltonian expressions used in the main text. We continue in the deep topological limit of the BBH model with $\lambda = 0$. Since the continuum Hamiltonian Eq. (11) is composed of linear operators in x , y , and matrices acting on the particle-hole τ , orbital σ , and spin s degrees of freedom, we can write a generic wavefunction as

$$\psi(x, y) = \sum_{\alpha} c_{\alpha} \phi^{\alpha}(x) \varphi^{\alpha}(y) \chi_{\alpha}, \quad (C1)$$

where ϕ^{α} (φ^{α}) is a complex spatial function of x (y), and χ_{α} are eight component spinors labelled by α . Using this form, we can obtain solutions that are localized on specific edges (or corners) by checking how the Hamiltonian acts individually in each part.

For the I and III edges, we look for localized solutions on x . We split $h_\Gamma = h_{0x} + h_{ky}$, where $h_{0x} = t\Gamma_2 + tk_x a\Gamma_3 + t\Gamma_4$ is the part which determine the zero states localized along x , while we treat $h_{ky} = tk_y a\Gamma_1 + \Delta\Gamma_5 + B_x\Gamma_6$ as its perturbation, reasonable given the fact that $B_x, \Delta \ll t$. Next we perform the substitution $k_x \rightarrow -i\partial_x$ and look for solutions of

$$h_{0x}\psi(x, y) = [t\Gamma_2 - it\partial_x a\Gamma_3 + t\Gamma_4]\psi(x, y) = 0. \quad (\text{C2})$$

Using the ansatz $\phi_\alpha(x) = \exp(q_x x/a)$ and that the χ_α are linearly independent, we get the matrix equations

$$[t\tau_3\sigma_2s_2 - itq_x\tau_3\sigma_2s_3 + t\tau_3\sigma_1s_0]\chi_\alpha = 0, \quad (\text{C3})$$

where we omit the external product for convenience. Multiplying the whole equation by $\tau_3 \otimes \sigma_2 \otimes s_2$ and dividing by t , we obtain

$$(\tau_0\sigma_0s_0 + q_x\tau_0\sigma_0s_1 - i\tau_0\sigma_3s_2)\chi_\alpha = 0, \quad (\text{C4})$$

which is diagonal in τ and σ , but not in s . The above equation has non-trivial solutions when the determinant

$$\left[\langle s_3 = 1 | + (m - \sqrt{2}) \langle s_3 = -1 | \right] s_1 \left[|s_3 = 1\rangle + (m' - \sqrt{2}) |s_3 = -1\rangle \right] = m + m' - 2\sqrt{2} \quad (\text{C7})$$

$$\left[\langle s_3 = 1 | + (m - \sqrt{2}) \langle s_3 = -1 | \right] s_2 \left[|s_3 = 1\rangle + (m' - \sqrt{2}) |s_3 = -1\rangle \right] = i(m - m'), \quad (\text{C8})$$

$$(\text{C9})$$

such that we get

$$tk_y a \chi_{lm}^\dagger \Gamma_1 \chi_{l'm'} = -tk_y a (\tau_3)_{l,l'} (\sigma_2)_{m,m'} \quad (\text{C10})$$

$$\Delta \chi_{lm}^\dagger \Gamma_5 \chi_{l'm'} = 0 \quad (\text{C11})$$

$$B_x \chi_{lm}^\dagger \Gamma_6 \chi_{l'm'} = -\frac{B_x}{\sqrt{2}} (\tau_3)_{l,l'} (\sigma_0)_{m,m'}, \quad (\text{C12})$$

where we use that the Γ_6 term vanishes because it is proportional to $(m - m') (\sigma_0)_{m,m'} = 0$. Combining all terms, we arrive at the edge Hamiltonian

$$h^I(k_y) = -tk_y a \tau_3 \otimes \sigma_2 - \frac{B_x}{\sqrt{2}} \tau_3 \otimes \sigma_0. \quad (\text{C13})$$

For the III edge, we instead need to use the solution $q_x = \sqrt{2}$. Performing an equivalent procedure to above, we obtain

$$\chi_{lm} = |\tau_3 = l\rangle \otimes |s_3 = m\rangle \otimes \frac{|s_3 = 1\rangle - (m + \sqrt{2}) |s_3 = -1\rangle}{\sqrt{4 + 2m\sqrt{2}}},$$

of the term between parenthesis is zero:

$$\begin{vmatrix} 1 & q_x - m \\ q_x + m & 1 \end{vmatrix} = 2 - q_x^2 = 0 \rightarrow q_x = \pm\sqrt{2}. \quad (\text{C5})$$

where $m = \pm 1$ is the eigenstate of σ_3 . Note that q_x does not depend on the eigenvalue l of τ_3 . A solution that is localized on the I edge should have negative q_x , while one localized on the III edge should have a positive q_x . Therefore, for the I edge, $q_x = -\sqrt{2}$, while for the III edge, $q_x = \sqrt{2}$.

Focusing first on the I edge, we write the localized solutions as

$$\chi_{l,m} = |l, m\rangle \otimes (a |s_3 = 1\rangle + b |s_3 = -1\rangle),$$

such that a and b are given by

$$\begin{pmatrix} 1 & -\sqrt{2} - m \\ -\sqrt{2} + m & 1 \end{pmatrix} \begin{pmatrix} a \\ b \end{pmatrix} = 0$$

$$\therefore b = (m - \sqrt{2}) a, \quad a = \sqrt{\frac{1}{4 - 2m\sqrt{2}}}, \quad (\text{C6})$$

where in the last equality, we used that $a^2 + b^2 = 1$. Next we add the other terms in the Hamiltonian of Eq. (11), to obtain the energy of the modes localized on the I edge by computing $\chi_{l,m}^\dagger h_{kyee} \chi_{l,m}$. For that, we notice that

and

$$h^{\text{III}}(k_y) = -tk_y a \tau_3 \otimes \sigma_2 - \frac{B_x}{\sqrt{2}} \tau_3 \otimes \sigma_0. \quad (\text{C14})$$

For the II and IV edges, the solutions should instead be localized on y . Therefore, we take $h_{0y} = t\Gamma_2 + tk_y a\Gamma_1 + t\Gamma_4$ to look for localized solutions and consider the perturbation to be $h_{ky} = tk_x a\Gamma_3 + \Delta\Gamma_5 + B_x\Gamma_6$, making $k_y \rightarrow -i\partial_y$, and look for solutions of

$$h_{0y}\psi(x, y) = [-it\partial_y a\Gamma_1 + t\Gamma_2 + t\Gamma_4]\psi(x, y) = 0. \quad (\text{C15})$$

Again, we use an ansatz $\varphi_\alpha(y) = \exp(q_y y/a)$ to obtain the matrix equation

$$[q_y\tau_0\sigma_0s_0 - \tau_0\sigma_0s_3 + \tau_0\sigma_3s_1]\chi_\alpha = 0, \quad (\text{C16})$$

after multiplying h_{0y} by $i/t\tau_3\sigma_2s_1$. In this way, q_y is determined by

$$\begin{vmatrix} q_y - 1 & m \\ m & q_y + 1 \end{vmatrix} = q_y^2 - 2 = 0 \rightarrow q_y = \pm\sqrt{2}. \quad (\text{C17})$$

The solution localized on the II edge is the one with $q_y = -\sqrt{2}$, and the one on the IV edge has $q_y = \sqrt{2}$. For the II edge, the solution is given by

$$\chi_{l,m} = |l, m\rangle \otimes \frac{|s_3 = 1\rangle - m(1 + \sqrt{2})|s_3 = -1\rangle}{\sqrt{4 + 2\sqrt{2}}},$$

and

$$h^{\text{II}}(k_x) = tk_x a \tau_3 \otimes \sigma_2 - \frac{1}{\sqrt{2}} B_x \tau_3 \otimes \sigma_3, \quad (\text{C18})$$

while for the IV edge, the solution is given by

$$\chi_{l,m} = |l, m\rangle \otimes \frac{|s_3 = 1\rangle + m(1 - \sqrt{2})|s_3 = -1\rangle}{\sqrt{4 + 2\sqrt{2}}},$$

and

$$h^{\text{IV}}(k_x) = tk_x a \tau_3 \otimes \sigma_2 - \frac{1}{\sqrt{2}} B_x \tau_3 \otimes \sigma_3. \quad (\text{C19})$$

-
- [1] A. Altland and M. R. Zirnbauer, Nonstandard symmetry classes in mesoscopic normal-superconducting hybrid structures, *Phys. Rev. B* **55**, 1142 (1997).
- [2] A. P. Schnyder, S. Ryu, A. Furusaki, and A. W. W. Ludwig, Classification of topological insulators and superconductors in three spatial dimensions, *Phys. Rev. B* **78**, 195125 (2008).
- [3] L. Fu, Topological crystalline insulators, *Phys. Rev. Lett.* **106**, 106802 (2011).
- [4] R.-J. Slager, A. Mesaros, V. Juričić, and J. Zaanen, The space group classification of topological band-insulators, *Nat. Phys.* **9**, 98 (2013).
- [5] J. Kruthoff, J. de Boer, J. van Wezel, C. L. Kane, and R.-J. Slager, Topological classification of crystalline insulators through band structure combinatorics, *Phys. Rev. X* **7**, 041069 (2017).
- [6] H. C. Po, A. Vishwanath, and H. Watanabe, Symmetry-based indicators of band topology in the 230 space groups, *Nat. Commun.* **8**, 50 (2017).
- [7] T. Neupert and F. Schindler, Topological crystalline insulators, *Topological Matter: Lectures from the Topological Matter School 2017*, 31 (2018).
- [8] W. A. Benalcazar, B. A. Bernevig, and T. L. Hughes, Electric multipole moments, topological multipole moment pumping, and chiral hinge states in crystalline insulators, *Phys. Rev. B* **96**, 245115 (2017).
- [9] W. A. Benalcazar, B. A. Bernevig, and T. L. Hughes, Quantized electric multipole insulators, *Science* **357**, 61 (2017).
- [10] F. Schindler, A. M. Cook, M. G. Vergniory, Z. Wang, S. S. Parkin, B. A. Bernevig, and T. Neupert, Higher-order topological insulators, *Science advances* **4**, eaat0346 (2018).
- [11] F. Schindler, Z. Wang, M. G. Vergniory, A. M. Cook, A. Murani, S. Sengupta, A. Y. Kasumov, R. Deblock, S. Jeon, I. K. Drozdov, *et al.*, Higher-order topology in bismuth, *Nat. Phys.* **14**, 918 (2018).
- [12] M. Ezawa, Higher-order topological electric circuits and topological corner resonance on the breathing kagome and pyrochlore lattices, *Phys. Rev. B* **98**, 201402 (2018).
- [13] G. van Miert and C. Ortix, Higher-order topological insulators protected by inversion and rotoinversion symmetries, *Phys. Rev. B* **98**, 081110 (2018).
- [14] W. A. Benalcazar, T. Li, and T. L. Hughes, Quantization of fractional corner charge in C_n -symmetric higher-order topological crystalline insulators, *Phys. Rev. B* **99**, 245151 (2019).
- [15] D. Călugăru, V. Juričić, and B. Roy, Higher-order topological phases: A general principle of construction, *Phys. Rev. B* **99**, 041301 (2019).
- [16] T. Nag, V. Juričić, and B. Roy, Out of equilibrium higher-order topological insulator: Floquet engineering and quench dynamics, *Phys. Rev. Res.* **1**, 032045 (2019).
- [17] W. A. Benalcazar and A. Cerjan, Bound states in the continuum of higher-order topological insulators, *Phys. Rev. B* **101**, 161116 (2020).
- [18] A. Agarwala, V. Juričić, and B. Roy, Higher-order topological insulators in amorphous solids, *Phys. Rev. Res.* **2**, 012067 (2020).
- [19] R. Arouca, S. N. Kempkes, and C. Morais Smith, Thermodynamics of a higher-order topological insulator, *Phys. Rev. Res.* **2**, 023097 (2020).
- [20] S. Saha, T. Nag, and S. Mandal, Multiple higher-order topological phases with even and odd pairs of zero-energy corner modes in a c_3 symmetry broken model, *Europhysics Lett.* **142**, 56002 (2023).
- [21] T. Nag, V. Juričić, and B. Roy, Hierarchy of higher-order floquet topological phases in three dimensions, *Phys. Rev. B* **103**, 115308 (2021).
- [22] A. K. Ghosh, T. Nag, and A. Saha, Systematic generation of the cascade of anomalous dynamical first- and higher-order modes in floquet topological insulators, *Phys. Rev. B* **105**, 115418 (2022).
- [23] D. Călugăru, V. Juričić, and B. Roy, Higher-order topological phases: A general principle of construction, *Phys. Rev. B* **99**, 041301 (2019).
- [24] R. Noguchi, M. Kobayashi, Z. Jiang, K. Kuroda, T. Takahashi, Z. Xu, D. Lee, M. Hirayama, M. Ochi, T. Shira-sawa, *et al.*, Evidence for a higher-order topological insulator in a three-dimensional material built from van der waals stacking of bismuth-halide chains, *Nat. Mater.* **20**, 473 (2021).
- [25] S. Imhof, C. Berger, F. Bayer, J. Brehm, L. W. Molenkamp, T. Kiessling, F. Schindler, C. H. Lee, M. Greiter, T. Neupert, *et al.*, Topoelectrical-circuit realization of topological corner modes, *Nat. Phys.* **14**, 925 (2018).
- [26] M. Serra-Garcia, R. Süssstrunk, and S. D. Huber, Observation of quadrupole transitions and edge mode topology in an lc circuit network, *Phys. Rev. B* **99**, 020304 (2019).

- [27] X. Ni, M. Weiner, A. Alù, and A. B. Khanikaev, Observation of higher-order topological acoustic states protected by generalized chiral symmetry, *Nat Mater.* **18**, 113 (2019).
- [28] H. Xue, Y. Yang, F. Gao, Y. Chong, and B. Zhang, Acoustic higher-order topological insulator on a kagome lattice, *Nat. Mater.* **18**, 108 (2019).
- [29] A. El Hassan, F. K. Kunst, A. Moritz, G. Andler, E. J. Bergholtz, and M. Bourennane, Corner states of light in photonic waveguides, *Nat. Photonics* **13**, 697 (2019).
- [30] S. Kempkes, M. Slot, J. van den Broeke, P. Capiod, W. Benalcazar, D. Vanmaekelbergh, D. Bercioux, I. Swart, and C. M. Smith, Robust zero-energy modes in an electronic higher-order topological insulator, *Nat. Mater.* **18**, 1292 (2019).
- [31] A. Cerjan, M. Jürgensen, W. A. Benalcazar, S. Mukherjee, and M. C. Rechtsman, Observation of a higher-order topological bound state in the continuum, *Phys. Rev. Lett.* **125**, 213901 (2020).
- [32] S. Zheng, X. Man, Z.-L. Kong, Z.-K. Lin, G. Duan, N. Chen, D. Yu, J.-H. Jiang, and B. Xia, Observation of fractal higher-order topological states in acoustic metamaterials, *Science Bulletin* **67**, 2069 (2022).
- [33] J. Li, Q. Mo, J.-H. Jiang, and Z. Yang, Higher-order topological phase in an acoustic fractal lattice, arXiv preprint arXiv:2205.05298 (2022).
- [34] Y. Wang, M. Lin, and T. L. Hughes, Weak-pairing higher order topological superconductors, *Phys. Rev. B* **98**, 165144 (2018).
- [35] A. K. Ghosh, T. Nag, and A. Saha, Floquet generation of a second-order topological superconductor, *Phys. Rev. B* **103**, 045424 (2021).
- [36] L. M. Vasiloiu, A. Tiwari, and J. H. Bardarson, Dephasing-enhanced majorana zero modes in two-dimensional and three-dimensional higher-order topological superconductors, *Phys. Rev. B* **106**, L060307 (2022).
- [37] Y. Wang, G. Rai, S. Haas, and A. Jagannathan, Edge and corner superconductivity in a two-dimensional topological model, *Phys. Rev. B* **107**, 104507 (2023).
- [38] A. K. Ghosh, T. Nag, and A. Saha, Hierarchy of higher-order topological superconductors in three dimensions, *Phys. Rev. B* **104**, 134508 (2021).
- [39] A. K. Ghosh, T. Nag, and A. Saha, Floquet generation of a second-order topological superconductor, *Phys. Rev. B* **103**, 045424 (2021).
- [40] A. K. Ghosh and T. Nag, Non-hermitian higher-order topological superconductors in two dimensions: Statics and dynamics, *Phys. Rev. B* **106**, L140303 (2022).
- [41] A. K. Ghosh, T. Nag, and A. Saha, Dynamical construction of quadrupolar and octupolar topological superconductors, *Phys. Rev. B* **105**, 155406 (2022).
- [42] B. Roy, Higher-order topological superconductors in \mathcal{P} -, \mathcal{T} -odd quadrupolar dirac materials, *Phys. Rev. B* **101**, 220506 (2020).
- [43] A. Y. Kitaev, Unpaired majorana fermions in quantum wires, *Physics-Uspekhi* **44**, 131 (2001).
- [44] R. M. Lutchyn, J. D. Sau, and S. Das Sarma, Majorana fermions and a topological phase transition in semiconductor-superconductor heterostructures, *Phys. Rev. Lett.* **105**, 077001 (2010).
- [45] Y. Oreg, G. Refael, and F. von Oppen, Helical liquids and majorana bound states in quantum wires, *Phys. Rev. Lett.* **105**, 177002 (2010).
- [46] V. Mourik, K. Zuo, S. M. Frolov, S. Plissard, E. P. Bakkers, and L. P. Kouwenhoven, Signatures of majorana fermions in hybrid superconductor-semiconductor nanowire devices, *Science* **336**, 1003 (2012).
- [47] S. Nadj-Perge, I. K. Drozdov, B. A. Bernevig, and A. Yazdani, Proposal for realizing majorana fermions in chains of magnetic atoms on a superconductor, *Phys. Rev. B* **88**, 020407 (2013).
- [48] S. Nadj-Perge, I. K. Drozdov, J. Li, H. Chen, S. Jeon, J. Seo, A. H. MacDonald, B. A. Bernevig, and A. Yazdani, Observation of majorana fermions in ferromagnetic atomic chains on a superconductor, *Science* **346**, 602 (2014).
- [49] L. Baldo, L. G. G. V. D. D. Silva, A. M. Black-Schaffer, and J. Cayao, Zero-frequency supercurrent susceptibility signatures of trivial and topological zero-energy states in nanowire junctions, *Superconductor Science and Technology* **36**, 034003 (2023).
- [50] O. A. Awoga, M. Leijnse, A. M. Black-Schaffer, and J. Cayao, Mitigating disorder-induced zero-energy states in weakly coupled superconductor-semiconductor hybrid systems, *Phys. Rev. B* **107**, 184519 (2023).
- [51] C. Nayak, S. H. Simon, A. Stern, M. Freedman, and S. Das Sarma, Non-abelian anyons and topological quantum computation, *Rev. Mod. Phys.* **80**, 1083 (2008).
- [52] T. Löfwander, V. S. Shumeiko, and G. Wendin, Andreev bound states in high- T_c superconducting junctions, *Superconductor Science and Technology* **14**, R53 (2001).
- [53] S. Ryu and Y. Hatsugai, Topological origin of zero-energy edge states in particle-hole symmetric systems, *Phys. Rev. Lett.* **89**, 077002 (2002).
- [54] A. P. Schnyder, P. M. R. Brydon, and C. Timm, Types of topological surface states in nodal noncentrosymmetric superconductors, *Phys. Rev. B* **85**, 024522 (2012).
- [55] S. Matsuura, P.-Y. Chang, A. P. Schnyder, and S. Ryu, Protected boundary states in gapless topological phases, *N. J. Phys.* **15**, 065001 (2013).
- [56] A. C. Potter and P. A. Lee, Edge ferromagnetism from majorana flat bands: Application to split tunneling-conductance peaks in high- T_c cuprate superconductors, *Phys. Rev. Lett.* **112**, 117002 (2014).
- [57] A. P. Schnyder and P. M. Brydon, Topological surface states in nodal superconductors, *J. Phys.: Condens. Matter* **27**, 243201 (2015).
- [58] D. Chakraborty, T. Löfwander, M. Fogelström, and A. M. Black-Schaffer, Disorder-robust phase crystal in high-temperature superconductors stabilized by strong correlations, *npj Quantum Materials* **7**, 44 (2022).
- [59] P. M. Bonetti, D. Chakraborty, X. Wu, and A. P. Schnyder, van hove, rashba, and hubbard meet to form first-order and higher-order topological superconductors, arXiv preprint arXiv:2304.07100 (2023).
- [60] H. Li and F. D. M. Haldane, Entanglement spectrum as a generalization of entanglement entropy: Identification of topological order in non-abelian fractional quantum hall effect states, *Phys. Rev. Lett.* **101**, 010504 (2008).
- [61] T. L. Hughes, E. Prodan, and B. A. Bernevig, Inversion-symmetric topological insulators, *Phys. Rev. B* **83**, 245132 (2011).
- [62] T. Fukui and Y. Hatsugai, Entanglement polarization for the topological quadrupole phase, *Phys. Rev. B* **98**, 035147 (2018).
- [63] Y. You, J. Bibo, and F. Pollmann, Higher-order entanglement and many-body invariants for higher-order topological phases, *Phys. Rev. Res.* **2**, 033192 (2020).

- [64] P. Zhu, K. Loehr, and T. L. Hughes, Identifying C_n -symmetric higher-order topology and fractional corner charge using entanglement spectra, *Phys. Rev. B* **101**, 115140 (2020).
- [65] D. Sticlet, C. Bena, and P. Simon, Spin and majorana polarization in topological superconducting wires, *Phys. Rev. Lett.* **108**, 096802 (2012).
- [66] C. Bena, Testing the formation of majorana states using majorana polarization, *Comptes Rendus Physique* **18**, 349 (2017).
- [67] M. Sato, Y. Takahashi, and S. Fujimoto, Non-abelian topological order in s -wave superfluids of ultracold fermionic atoms, *Phys. Rev. Lett.* **103**, 020401 (2009).
- [68] W. P. Su, J. R. Schrieffer, and A. J. Heeger, Solitons in polyacetylene, *Phys. Rev. Lett.* **42**, 1698 (1979).
- [69] P. Zhu, K. Loehr, and T. L. Hughes, Identifying C_n -symmetric higher-order topology and fractional corner charge using entanglement spectra, *Phys. Rev. B* **101**, 115140 (2020).
- [70] R. D. King-Smith and D. Vanderbilt, Theory of polarization of crystalline solids, *Phys. Rev. B* **47**, 1651 (1993).
- [71] R. Resta, Quantum-mechanical position operator in extended systems, *Phys. Rev. Lett.* **80**, 1800 (1998).
- [72] N. A. Spaldin, A beginner's guide to the modern theory of polarization, *Journal of Solid State Chemistry* **195**, 2 (2012).
- [73] K. G. Wilson, Confinement of quarks, *Phys. Rev. D* **10**, 2445 (1974).
- [74] L. Herviou, N. Regnault, and J. H. Bardarson, Entanglement spectrum and symmetries in non-hermitian fermionic non-interacting models, *SciPost Physical* **7**, 069 (2019).
- [75] C. Ortega-Taberner, L. Rødland, and M. Hermanns, Polarization and entanglement spectrum in non-hermitian systems, *Phys. Rev. B* **105**, 075103 (2022).
- [76] T. L. Hughes, E. Prodan, and B. A. Bernevig, Inversion-symmetric topological insulators, *Phys. Rev. B* **83**, 245132 (2011).
- [77] Y. You, J. Bibo, and F. Pollmann, Higher-order entanglement and many-body invariants for higher-order topological phases, *Phys. Rev. Res.* **2**, 033192 (2020).
- [78] A. Maiellaro, J. Settimo, C. Guarcello, F. Romeo, and R. Citro, Hallmarks of orbital-flavored majorana states in josephson junctions based on oxide nanochannels, *Phys. Rev. B* **107**, L201405 (2023).
- [79] M. Vojta, Quantum phase transitions, *Rep. Prog. Phys.* **66**, 2069 (2003).
- [80] H. Ma, Z. Zhang, P.-H. Fu, J. Wu, and X.-L. Yu, Electronic and topological properties of extended two-dimensional su-schrieffer-heeger models and realization of flat edge bands, *Phys. Rev. B* **106**, 245109 (2022).
- [81] B. Wang, X. Zhou, H. Lin, and A. Bansil, Higher-order topological insulator phase in a modified haldane model, *Phys. Rev. B* **104**, L121108 (2021).
- [82] S. A. A. Ghorashi, T. Li, and T. L. Hughes, Higher-order weyl semimetals, *Phys. Rev. Lett.* **125**, 266804 (2020).
- [83] X. Zhang, Z.-K. Lin, H.-X. Wang, Z. Xiong, Y. Tian, M.-H. Lu, Y.-F. Chen, and J.-H. Jiang, Symmetry-protected hierarchy of anomalous multipole topological band gaps in nonsymmorphic metacrystals, *Nature Communications* **11**, 65 (2020).
- [84] Y. Yang, J. Lu, M. Yan, X. Huang, W. Deng, and Z. Liu, Hybrid-order topological insulators in a phononic crystal, *Phys. Rev. Lett.* **126**, 156801 (2021).
- [85] Z. Wang, X. Wang, Z. Hu, D. Bongiovanni, D. Jukić, L. Tang, D. Song, R. Morandotti, Z. Chen, and H. Buljan, Sub-symmetry-protected topological states, *Nature Physics* **19**, 992 (2023).
- [86] M. S. Hossain, F. Schindler, R. Islam, Z. Muhammad, Y.-X. Jiang, Z.-J. Cheng, Q. Zhang, T. Hou, H. Chen, M. Litskevich, *et al.*, Discovery of a hybrid topological quantum state in an elemental solid, arXiv preprint arXiv:2401.04845 (2024).
- [87] R. Jackiw and C. Rebbi, Solitons with fermion number $\frac{1}{2}$, *Phys. Rev. D* **13**, 3398 (1976).
- [88] C. J. Lapp, J. M. Link, and C. Timm, Complete zero-energy flat bands of surface states in fully gapped chiral noncentrosymmetric superconductors, arXiv preprint arXiv:2310.14800 (2023).